



NRL/MR/6770--14-9554

Proof of Principle for Active Detection of Fissionable Material Using Intense, Pulsed-Bremsstrahlung-Induced Photofission

R.J. COMMISSO
J.W. SCHUMER
R.J. ALLEN
D.D. HINSHELWOOD
S.L. JACKSON
D.P. MURPHY
S.B. SWANEKAMP
B.V. WEBER
J.C. ZIER

*Pulsed Power Physics Branch
Plasma Physics Division*

J.P. APRUZESE
G. COOPERSTEIN
D. MOSHER
P.F. OTTINGER
F.C. YOUNG

*Engility Inc.
Chantilly, Virginia*

B.F. PHILIPS
A.L. HUTCHESON
W.N. JOHNSON
L.J. MITCHELL
E.A. WULF

*High-Energy Space Environment Branch
Space Sciences Division*

R.S. WOOLF
NATIONAL RESEARCH COUNCIL RESEARCH ASSOCIATE
*High-Energy Space Environment Branch
Space Sciences Division*

A.W. HUNT
Z.M. LARSEN
E.S. CARDENAS
*Idaho State University
Idaho Falls, ID 83415*

October 7, 2014

REPORT DOCUMENTATION PAGE				Form Approved OMB No. 0704-0188	
Public reporting burden for this collection of information is estimated to average 1 hour per response, including the time for reviewing instructions, searching existing data sources, gathering and maintaining the data needed, and completing and reviewing this collection of information. Send comments regarding this burden estimate or any other aspect of this collection of information, including suggestions for reducing this burden to Department of Defense, Washington Headquarters Services, Directorate for Information Operations and Reports (0704-0188), 1215 Jefferson Davis Highway, Suite 1204, Arlington, VA 22202-4302. Respondents should be aware that notwithstanding any other provision of law, no person shall be subject to any penalty for failing to comply with a collection of information if it does not display a currently valid OMB control number. PLEASE DO NOT RETURN YOUR FORM TO THE ABOVE ADDRESS.					
1. REPORT DATE (DD-MM-YYYY) 07-10-2014		2. REPORT TYPE Memorandum Report		3. DATES COVERED (From - To) May 2010 – September 2012	
4. TITLE AND SUBTITLE Proof of Principle for Active Detection of Fissionable Material Using Intense, Pulsed-Bremsstrahlung-Induced Photofission				5a. CONTRACT NUMBER	
				5b. GRANT NUMBER	
				5c. PROGRAM ELEMENT NUMBER	
6. AUTHOR(S) R.J. Commisso, J.W. Schumer, R.J. Allen, D.D. Hinshelwood, S.L. Jackson, D.P. Murphy, S.B. Swanekamp, B.V. Weber, J.C. Zier, J.P. Apruzese, ¹ G. Cooperstein, ¹ D. Mosher, ¹ P.F. Ottinger, ¹ F.C. Young, ¹ B.F. Philips, A.L. Hutcheson, W.N. Johnson, L.J. Mitchell, E.A. Wulf, R.S. Woolf, ² A. W. Hunt, ³ Z.M. Larsen, ³ and E.S. Cardenas ³				5d. PROJECT NUMBER	
				5e. TASK NUMBER	
				5f. WORK UNIT NUMBER 67-9750-04 and 67-9345-A3	
7. PERFORMING ORGANIZATION NAME(S) AND ADDRESS(ES) Naval Research Laboratory, Code 6770 4555 Overlook Avenue, SW Washington, DC 20375-5320				8. PERFORMING ORGANIZATION REPORT NUMBER NRL/MR/6770--14-9554	
9. SPONSORING / MONITORING AGENCY NAME(S) AND ADDRESS(ES) Defense Threat Reduction Agency 8725 John Kingman Road Ft. Belvoir, VA 22060 Office of Naval Research One Liberty Center 875 North Randolph Street, Suite 1425 Arlington, VA 22203-1995				10. SPONSOR / MONITOR'S ACRONYM(S) DTRA and ONR	
				11. SPONSOR / MONITOR'S REPORT NUMBER(S)	
12. DISTRIBUTION / AVAILABILITY STATEMENT Approved for public release; distribution is unlimited.					
13. SUPPLEMENTARY NOTES ¹ Engility Inc., Chantilly, VA 20151 ² National Research Council Research Associate ³ Idaho Accelerator Center, Idaho State University, Idaho Falls, ID 83415					
14. ABSTRACT Photons of the appropriate energy can induce photofission in fissile material. We are investigating the applicability of this mechanism, using photons from bremsstrahlung, for long-range (~ 100 m) detection of fissile material using high-power (~ 1 TW), pulsed technology—so called intense, pulsed active detection. In this report, we describe the results of laboratory, proof-of-principle experiments, supported by computations and analyses, in which a single pulse of 8-MeV endpoint bremsstrahlung from the Naval Research Laboratory Mercury pulsed-power generator (200-kA peak current, 50-ns pulse width) induces photofission in depleted uranium. Fission products are measured using He-3 proportional counters, and plastic (BC408), sodium-iodide (NaI:TI), and bismuth-germinate-oxide scintillators. Prompt neutrons, delayed neutrons, and delayed gamma-rays from the induced photofission are measured unambiguously. Delayed neutron and gamma-ray measurements are also carried out with various thicknesses of low- and high-atomic-number materials attenuating the bremsstrahlung and fission signatures. Results of simulations and analyses carried out in support of the experiments are in agreement with the measurements. In addition, we demonstrate that relatively simple variations of the diode geometry can increase the efficiency of inducing fissions three-fold over the original geometry. These geometry changes cause the electron beam to be more normally incident onto the tantalum converter and thereby increase the forward-directed bremsstrahlung intensity without changing the driving, electrical power pulse. The results of this work and future directions for this research are presented in this report.					
15. SUBJECT TERMS Active detection of fissile material Bremsstrahlung Photofission Pulsed power					
16. SECURITY CLASSIFICATION OF:			17. LIMITATION OF ABSTRACT Unclassified Unlimited	18. NUMBER OF PAGES 32	19a. NAME OF RESPONSIBLE PERSON R.J. Commisso
a. REPORT Unclassified Unlimited	b. ABSTRACT Unclassified Unlimited	c. THIS PAGE Unclassified Unlimited			19b. TELEPHONE NUMBER (include area code) (202) 404-8984

CONTENTS

1. INTRODUCTION	1
2. RADIATION SOURCE AND MERCURY PULSED POWER	3
3. DELAYED γ -RAY MEASUREMENTS	5
4. DELAYED NEUTRON MEASUREMENTS	8
5. PROMPT NEUTRON MEASUREMENTS	12
6. DETECTION STUDIES WITH MASS ATTENUATION	16
7. DIODE IMPROVEMENTS	19
8. SUMMARY AND CONCLUSIONS	23
9. ACKNOWLEDGMENTS	24
10. REFERENCES	25

1. INTRODUCTION

Passive and active detection of hidden fissile material is a subject of intense interest.^{1,2} In active detection, the strength of the characteristic radiations associated with naturally occurring fission are significantly enhanced so that these signatures are more readily measured compared with the passive approach that measures what can be relatively weak and easily-attenuated radiations associated with the natural decay (i.e., α -decay) of fissile material.^{2,3,4} One approach to active detection utilizes the bremsstrahlung produced when an electron beam strikes a high-atomic-number material. Photons of about 6 MeV and higher can induce photofission in fissile material to produce detectable fission products. This approach was pioneered^{2,5,6,7,8,9} and is still being pursued¹⁰ using a pulse train of bremsstrahlung pulses produced by a linear accelerator (linac), commonly used for medical applications. The linac approach is attractive because it employs nearly-commercial-off-the-shelf, compact technology. However, because of the relatively low current associated with linacs (usually less than 1 mA average current), it can take several minutes of bremsstrahlung irradiation at relatively high electron endpoint energy (20 MeV or higher) to induce sufficient fissions for long-standoff detection applications (~ 100 m). The relatively long measurement time can be a disadvantage in a practical application. While the high endpoint-energy of the linac approach results in more photons emitted per electron near the maximum of the photofission cross section (~ 14 MeV)¹¹ than with moderate-endpoint-energy photons (e.g., 8-12 MeV), the resulting high-energy photons can induce collateral photo-activation of the environment and other benign materials in the photon beam path.^{12,13} The resulting induced (active) background radiation can severely complicate a high-confidence measurement of the fission signature. Also, a significant natural (passive) background (e.g. from cosmic rays) can accumulate with long measurement time.

An alternative to the linac approach relies on the use of TW-level pulsed-power technology, similar to that used in laboratory simulation of nuclear weapon effects.¹⁴ The complete measurement of a fission signature made after a single pulse is generally termed intense, pulsed, active detection (IPAD).¹⁵ The high-power electrical pulse is used to create a short (~ 100 ns), intense, bremsstrahlung pulse that induces photo-fission in fissile material.^{15,16,17,18} The IPAD approach has the potential advantage of being able to measure within a few seconds after the pulse both the prompt neutron signature as well as the beta-delayed neutron and γ -ray signatures associated with the induced photo-fissions. Prompt neutrons may be detected within a few hundred nanoseconds after the irradiation pulse, depending on the detector distance. The much shorter measurement time of the IPAD technique reduces the natural background signal to a much smaller fraction of the measured signal than obtained with a conventional, repetitively-pulsed linac approach.¹⁵ However, progress is required: (1) to develop detectors that recover promptly from the scattered radiation associated with the interrogating pulse, (2) to minimize the induced background (i.e., by using moderate-energy bremsstrahlung),^{12,13,15} and (3) to make pulsed-power driver technology more robust and compact.^{19,20}

Earlier IPAD experiments^{21,22} used 6- to 7-MeV characteristic gamma-rays produced via the $^{19}\text{F}(p,\alpha\gamma)^{16}\text{O}$ nuclear reaction to induce fission in a depleted uranium (DU) object.²³ An intense characteristic γ -ray pulse was produced with the Naval Research Laboratory Mercury inductive voltage adder (IVA)²⁴ operated in positive polarity²⁵ to generate an intense proton beam²⁶ that bombarded a fluorinated target (CF_2). The characteristic gamma-rays induced fission in a DU object, and fission neutrons were measured. The results are reported in Refs. 21 and 22. While products from induced fission were measured using this technique, the low efficiency of characteristic gamma ray production and their inherent isotropic emission preclude application of this approach to long distance (~ 100 -m) standoff.

Early experimental investigations of the IPAD approach with moderate energy bremsstrahlung and analyses of these experiments are presented in this report. For these

experiments, Mercury was modified to increase its operating voltage from 6 to 8 MV (with 200-kA peak current and 50-ns electrical pulse width).²⁷ The 8-MeV bremsstrahlung from Mercury irradiated a 30-cm \times 30-cm \times 2.5-cm-thick DU plate from which fission products, including prompt neutrons, delayed neutrons, and delayed γ -rays, were measured.^{16,17,18} Delayed γ -rays were measured with bismuth-germinate-oxide (BGO) and sodium-iodide (NaI:TI) scintillator detectors. Measurement of a prompt- γ fission signature was assumed unachievable because of the much more intense scattered bremsstrahlung in the same spectral band and essentially at the same time. Delayed neutrons were measured with He-3 proportional counters. Prompt neutrons were measured with a fast-time-response plastic-scintillator detector to separate neutrons from photons (scattered bremsstrahlung) by virtue of their time-of-flight difference. Unambiguous signatures of induced fission were obtained from the delayed γ -rays measurements and from both the delayed and prompt neutron measurements.

Analytic and computational analyses were used to interpret the measurements and guide the experiments. The large-scale-plasma (LSP) particle-in-cell code²⁸ was used to model the dynamics of electron flow in the Mercury IVA and the electron beam (e-beam) dynamics in the diode. The integrated tiger series (ITS) Monte Carlo electron-photon transport code²⁹ was used to model bremsstrahlung production and transport. The Monte-Carlo N-particle extended (MCNPX) code³⁰ was used to model relevant nuclear reactions, neutron generation, and neutron transport. The measurements are also useful in benchmarking these codes.¹⁶⁻¹⁸

Measurements of delayed neutrons and γ -rays from induced fission also were carried out with materials interspersed between the DU plate and the bremsstrahlung source. Various thicknesses of low- and high-atomic-number (low- and high-Z) materials were used in these studies, as well as composites of low- and high-Z materials. Fission signals equal to or greater than 3 times the background standard deviation are obtained with up to 160 g/cm² areal mass density of high-Z attenuating material. Simulations of the fission signatures after radiation transport through various areal mass densities of attenuating material are in general agreement with the measured fission signatures.

In addition to these fission signature measurements, other experiments demonstrate an increase in the bremsstrahlung intensity on the DU plate by a factor-of-three. This is accomplished by adjusting the anode-cathode (AK) gap and the diameter of the outer conductor in the e-beam-diode region to make the electron trajectories striking the tantalum converter more normally incident, thereby increasing the radiation intensity in the forward direction.

All of these results are discussed in more detail in the following sections of this report.

2. RADIATION SOURCE AND MERCURY PULSED POWER

The design and modeling of the bremsstrahlung diode are described in detail in Ref. 17. The front end of the Mercury IVA is illustrated in Fig. 1, where the outputs of the generator cavities (not shown) are connected to the load via a magnetically insulated transmission line (MITL).³¹ A brief description of the initial diode geometry follows. The 17-cm diameter cylindrical MITL center conductor on the Mercury generator is at negative high voltage and is terminated in a 17-cm diameter hemisphere. A relatively large axial AK gap is used to minimize electron emission from the hemisphere so that the load presents a high impedance to the machine and the MITL fixes the effective load impedance to its self-limited impedance.^{32,33,34,35} Thus, the voltage is fixed at 8 MV and a significant fraction of the electron current incident on the anode tantalum converter comprises MITL flow electrons (or vacuum-flow current) emitted from along the MITL center conductor in what is called “self-limited” or “line-limited” flow.^{34,35} In Fig. 1, the 38-cm-diameter converter is located 23 cm from the tip of the hemisphere on the center conductor. Because of this large axial gap, the end of the MITL acts as a radial diode emitting

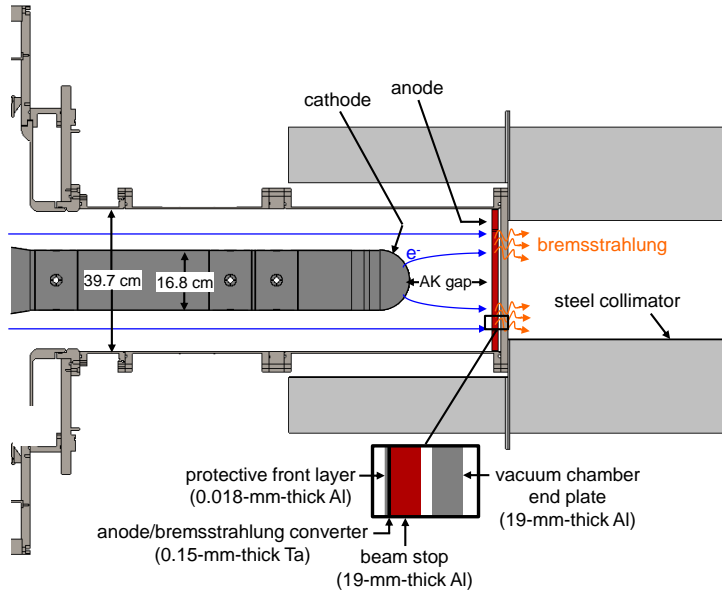


Figure 1. Schematic of the Mercury IVA front end and bremsstrahlung diode. The AK gap shown is 23 cm.

the remainder of the load current. This diode-emitted electron current joins the MITL flow current and this combined total electron current strikes the converter. All the data described in Secs. 3 through 5 were taken with this 23-cm diode AK gap. The data in Sec. 6 were taken with a 40-cm AK gap. Section VII describes diode improvement work where the AK gap is varied to optimize the electron angles of incidence on the Ta converter. The Ta converter thickness in all of the experiments is only 150- μ m (much less than optimum for maximum dose) and has an

aluminum beam-stop. This converter geometry optimizes the ratio of higher energy photons that induce photofission to lower energy photons that produce unwanted dose.¹⁷

To minimize the possibility of ion-beam production in the diode, the large-radius hemisphere is used to terminate the MITL so as to reduce the emitted e-beam current density and associated deposition heating of the anode surface. The converter is also covered with a thin (18- μ m thick) bare Al front layer both because Al has a higher thermal threshold for anode plasma formation and little beam energy is deposited within its thin layer. By avoiding anode plasma formation, which would result in ion-beam generation and partial space-charge neutralization of the e-beam, minimal e-beam focusing (or pinching) occurs in the diode, as desired. This front Al layer also prevents ions that form on the Ta converter from entering the vacuum diode region. However, as discussed below, these procedures, while preventing anode plasma formation, do not totally eliminate ions from the diode region.

To provide multiple reproducible shots without opening the system, the cathode and outer anode conductors were not coated with the usual thin graphite layer (e.g., using Aerodag³⁶), but instead are bare Al surfaces. Multiple shots with reproducible current and voltage waveforms are

achieved without opening the system as reported in Ref. 17. A thick steel collimator (20-cm thick upstream of the converter, 30-cm thick downstream of the converter) surrounds the diode to attenuate off-axis bremsstrahlung (see Fig. 1). This collimator has a 33-cm-diameter downstream bore and reduces the off-axis dose (angles $> 20^\circ$) by more than an order of magnitude.¹⁷

Diode performance including load current, load voltage, and bremsstrahlung production are described in Ref. 17. The electron dynamics of the diode region, including both vacuum-flow electrons from along the length of the MITL and electrons generated in the radial diode at the end of the MITL (see above), are modeled with the LSP particle-in-cell code, and the results compared with various measurements. As shown in Fig. 2, the calculated (total) load-current, I_{load} , and load-voltage, V_{load} , waveforms are in agreement with the measured waveforms. These quantities are measured at the end of the MITL before the hemisphere. Also shown in Fig. 2 is a measured bremsstrahlung pulse associated with the electrical pulse. In the simulations, the electron flow in the diode is modified by a small amount of ion charge created at the anode

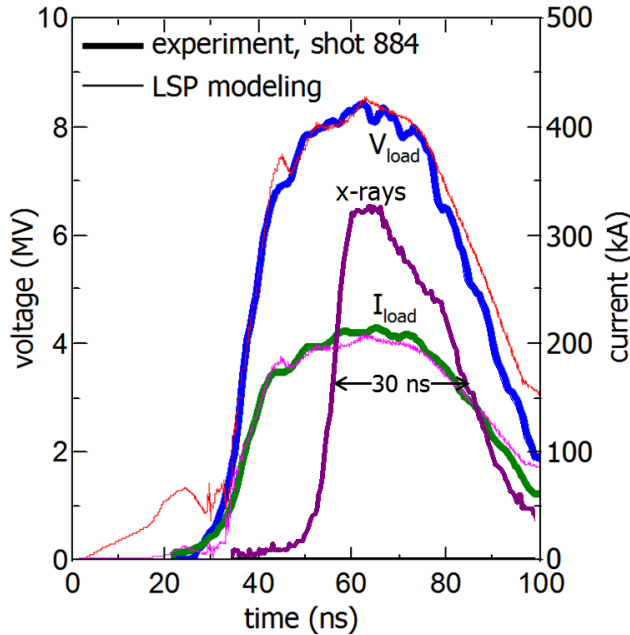


Figure 2. Comparison of experimental (thick lines) and LSP-computed (thin lines) load voltage and total current waveforms for the Mercury bremsstrahlung diode. Also shown is the experimental photodiode x-ray waveform (arbitrary scale).

simulations (discussed in what flows) suggest that this bremsstrahlung pulse induces about $2.25 \times 10^9 / [R_{\text{SO}}(\text{m})]^2$ fissions in the DU plate when it is a distance $R_{\text{SO}}(\text{m})$ from the bremsstrahlung converter.

surface by stimulated emission resulting from electron impact.³⁷ This stimulated ion emission in a given area is determined by setting an ion emission fraction in terms of ions emitted per incident electrons in that area. Stimulated ion emission fractions ranging from 0.2% to 0.6% are shown to have a substantial impact on the electron distribution and angles of incidence at the converter,¹⁸ and, as a result, on the forward-going bremsstrahlung intensity. The issue of the ion fraction will be discussed further in Sec. 4, below.

The dose associated with the bremsstrahlung pulse shown in Fig. 2 (and for the 23-cm AK gap) at 5 m from the bremsstrahlung converter is typically 20 rad (CaF_2). Various

3. DELAYED γ -RAY MEASUREMENTS

The arrangement for the delayed-gamma-ray measurements is illustrated in Fig. 3. The DU plate is located along the Mercury center line 5 m from the bremsstrahlung source but tilted at a 45° angle to center line. As shown in Fig. 3, the BGO detector is located 2.65 m from the DU plate and consists of six 5-cm diam by 5-cm thick BGO scintillators with photomultipliers mounted in a 3 × 2 array. Each detector was collimated with lead and 30%-borated polyethylene to partially mitigate stray photon and room-scattered neutron background. Individual pulses are

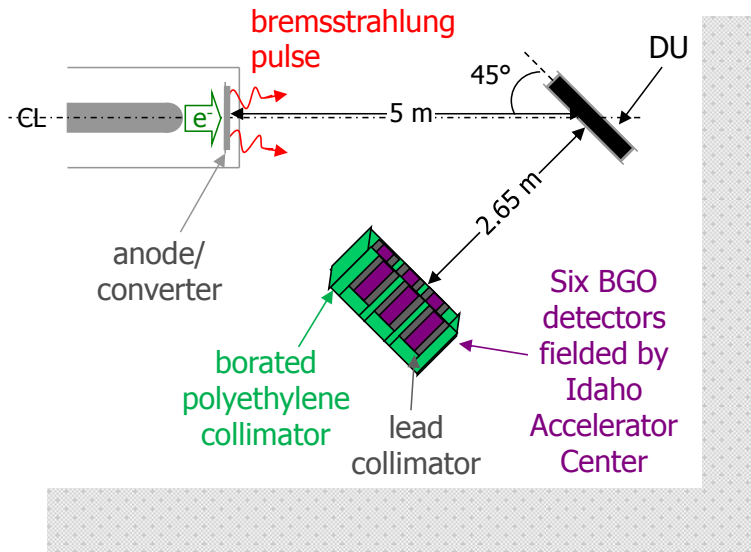


Figure 3. Top view of the bremsstrahlung diode, DU plate and BGO detectors for delayed γ -ray measurements.

recorded in list mode. The pulses can be summed in various time bins to provide the count rate as a function of time. Also, the pulse height is used to separate the counts into two broad γ -ray energy ranges: a broad, low-energy-cutoff range with $E_\gamma > 350$ keV, and a high-energy range with $3 \text{ MeV} < E_\gamma < 6 \text{ MeV}$. The 350-keV cutoff energy is selected to avoid detecting the 140-keV γ -ray from $^{75\text{m}}\text{Ge}$ (47-s half-life), which is produced by neutron activation in the BGO detector. The 3-

MeV cutoff energy is selected to eliminate the naturally occurring 2.614-MeV γ -ray from ^{208}Tl (in the decay chain of ^{208}Th).

Comparisons of measurements with the DU plate and a lead surrogate are presented in Fig. 4 for the broad, low-energy-cutoff γ -rays (Figs. 4a and 4c) and for the high-energy γ -rays (Figs. 4b and 4d). In Figs. 4a and 4b, the counts in each energy range are summed in 2-ms bins from 1 ms to 0.1 s and are plotted as a function of time at the center of each bin. In Figs. 4c and 4d, the counts in each energy range are summed in 20-ms bins from 1 ms to 1 s and are plotted as a function of time at the center of each bin. The error bars on the counts in these figures are statistical uncertainties. At early time in Figs. 4a and 4b, both the DU and the lead counts increase as the high voltage on the photomultiplier tube begins to recover from the intense bremsstrahlung pulse. After this 4- to 6-ms detector recovery, both the low-energy-cut and the high-energy-range counts decrease in similar fashion. At this time, however, the high-energy-range counts are about four-to-five times smaller than the low energy counts. This is expected because of fewer photons and lower detector efficiency for higher-energy delayed γ -rays.

As seen in Figs. 4(a) and (c), the induced (active) background measured with the lead surrogate in the first 20 to 30 ms masks the beta-delayed γ -ray signature from the DU fission products for both the broad-low-energy-cutoff and high-energy-range cases. This background persists for too long to be associated with room-scattered bremsstrahlung from the bremsstrahlung interrogating pulse (~ 30 -ns FWHM, see Fig. 2). However, bremsstrahlung can

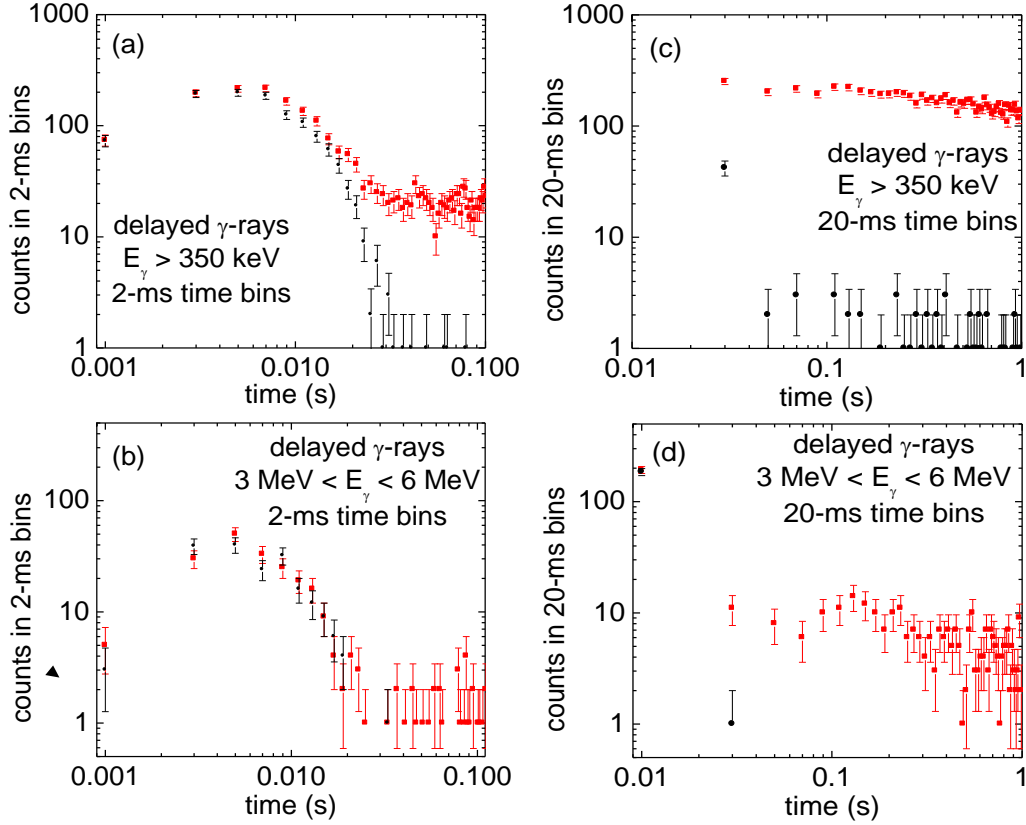


Figure 4. Delayed γ -ray counts plotted for the low energy cutoff in (a) and (c) and for the high-energy range in (b) and (d). The red squares are for shot 821 with the DU plate, and the black circles are for shot 823 with the lead surrogate. The counts are summed in 2-ms time bins in (a) and (b) and in 20-ms time bins in (c) and (d).

interact with the local environment to produce neutrons through photonuclear, (γ, n) , reactions. These neutrons may then thermalize and be captured by nuclei in the environment. These nuclei subsequently undergo (n, γ) reactions that produce short-lived γ -ray activity in materials comprising the entire environment as well as material surrounding the detector. Also, about 10^9 neutrons, produced in the e-beam diode, may contribute to this neutron-induced, background γ -ray activity.¹⁷ This process can last for as long as the photo neutrons take to thermalize, ~ 10 ms (or longer) similar to the time scale indicated in Figs. 4(a) and (c) for the active delayed-gamma background.

The DU and lead surrogate measurements are compared at later time using the 20-ms time bins in Figs. 4(c) and (d). After about 40 ms, the DU counts plateau at about 200 counts per bin for the low-energy-cutoff case (Fig. 4(c)) and less than 10 counts per bin for the high-energy-range case (Fig. 4(d)). The sums of the low-energy-cutoff counts from 40 ms to 1 s are 7840 counts with DU and 49 counts with lead, corresponding to a ratio of 160. For the high-energy cut, these sums over the same time period are 280 counts with DU and no counts with lead.

Clearly, unambiguous detection of the DU can be achieved within 1 s using a single, intense pulse. The low background associated with the high-energy γ -rays can be advantageous when quantifying detection confidence.

4. DELAYED NEUTRON MEASUREMENTS

Delayed neutrons are detected with an array of five He-3 proportional counters. The setup for these measurements is illustrated in Fig. 5. These detectors are encased in polyethylene, cadmium, and borated rubber to emphasize their response to the delayed neutron fission spectrum

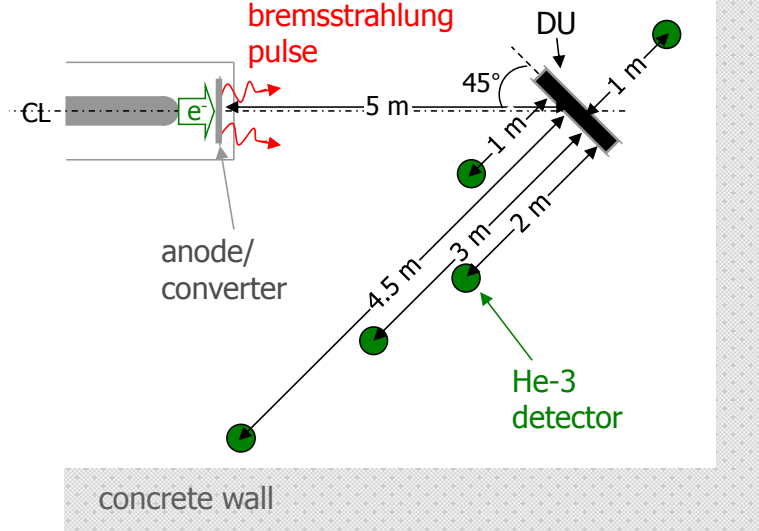


Figure 5. Top view of the arrangement of five He-3 detectors, the DU plate, and the bremsstrahlung diode for delayed neutron measurements.

relative to lower energy neutrons. The design and shielding of these detectors are described in detail in Refs. 22, 38, and 39. As shown in Fig. 5, the five detectors are located at distances ranging from 1 m to 4.5 m from the DU plate and the DU plate is on the Mercury center line 5 m from the bremsstrahlung source and tilted at a 45° angle to the center line. Large pulses are produced by low energy neutrons due to

the positive Q-value (0.762 MeV) of the $^3\text{He}(n,p)^3\text{H}$ reaction in the detector.

The first 100 ms of neutron pulses after the bremsstrahlung pulse, measured using the He-3 detector located 1 m from the front face of the DU, are compared in Fig. 6 for shots with DU, with lead only, and with no object. For these data, the detectors recover from the bremsstrahlung flash in 10 ms or less. Many neutron pulses are measured with the DU, but no neutron pulses are measured with either the lead surrogate or no object. For this case, summing the pulses recorded with the DU in 100 ms could provide a clear delayed-neutron signal with essentially no active background. This time scale is so short that the passive background is negligible (the passive background count rate at Mercury for this type of detector is about 0.024 counts/s). This low passive background contribution to the measurement is an inherent advantage of the IPAD approach.

Figure 7 shows a comparison of the counts recorded on the He-3 detector located 1 m behind the DU (see Fig. 5) summed in 30-ms time bins as a function of time for a shot with the DU plate, a shot with the lead surrogate, and a normalized fit of the 6-exponent decay model for DU photofission.⁴⁰ The data with lead show one count early in time (possibly from lead photo-neutrons) and one late in time. The DU data are in agreement with the decay model.

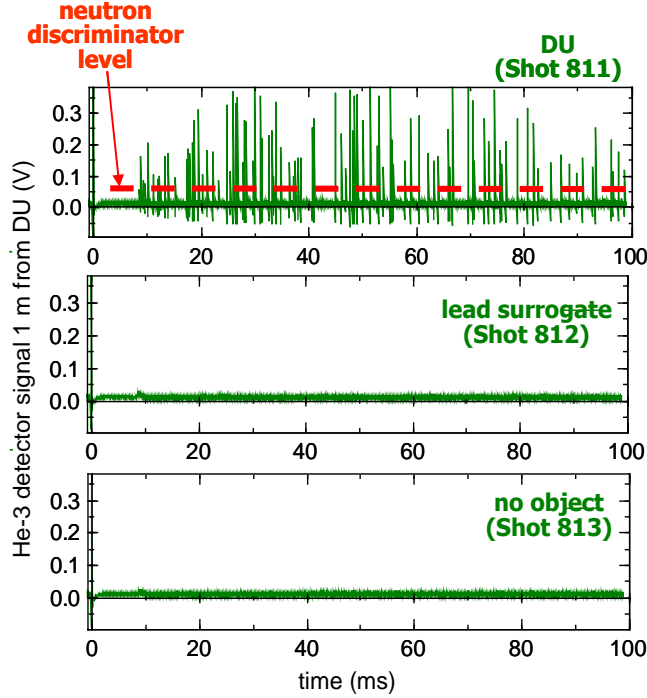


Figure 7. Signals from the He-3 detector located 1 m from the front face of the DU plate. Measurements with the DU plate (shot 811), the lead surrogate (shot 812) and no object (shot 813) are shown.

of the Mercury cell.¹⁶ These calculations are represented by the black squares in Fig. 8. The He-3 counts, measured over only 100 s, are corrected to saturation at 200 s using the 6-exponent-decay model⁴⁰ and averaged over three shots for each detector distance. MCNPX is used again to convert these measured He-3 counts into inferred incident delayed-neutron fluence.^{16,18} for comparison with the computed fluence. The previously-calculated spectrally dependent incident neutron fluence, including the scattered delayed-neutron contribution, must be used for this conversion as the absolute detector response³⁹ is neutron-energy dependent. These data are plotted as red diamonds in Fig. 8. Folding in the detector area,²² each He-3 detector count at 1-m from the DU plate is associated with about 8.9×10^4 induced fissions in the DU plate. The error bars on these data

In Fig. 8, the calculated neutron fluence incident on the He-3 detectors as a function of distance from the DU plate (see Fig. 5) is compared with the neutron fluence inferred from the measured pulses. The bremsstrahlung spectrum incident on the DU plate is calculated with LSP/ITS assuming a constant 0.4% ion fraction for stimulated emission (see Sec. 2). Then using the photon spectrum as input, MCNPX is used to calculate the neutron spectrum emitted from the DU and transported to each He-3 detector. This calculation includes the delayed neutrons from the induced fission in the DU plate as well as the contribution from the (induced-fission) neutrons that reflect off the composition-specific concrete walls, floor, and ceiling

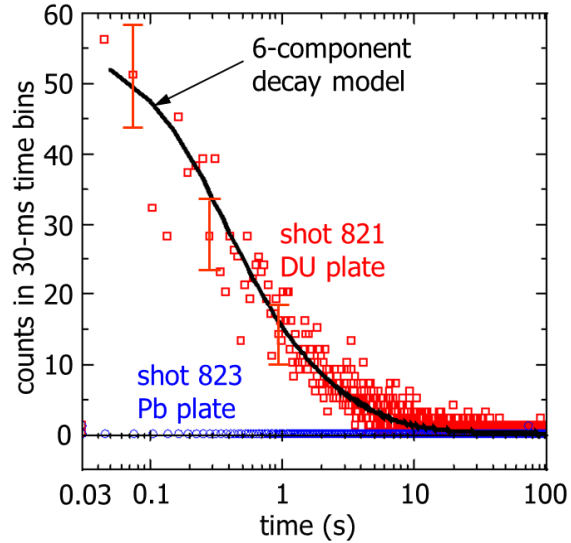


Figure 6. He-3 detector counts in 30-ms bins vs. time for shot 821 with the DU plate (red squares), and shot 823 with the lead surrogate (blue circles). The DU data are compared with the 6-component-decay model for photofission. Representative error bars indicate statistical uncertainty. The lead data show a total of 2 counts: one before 0.03 s and one at 74 s (i.e., most data points are at zero).

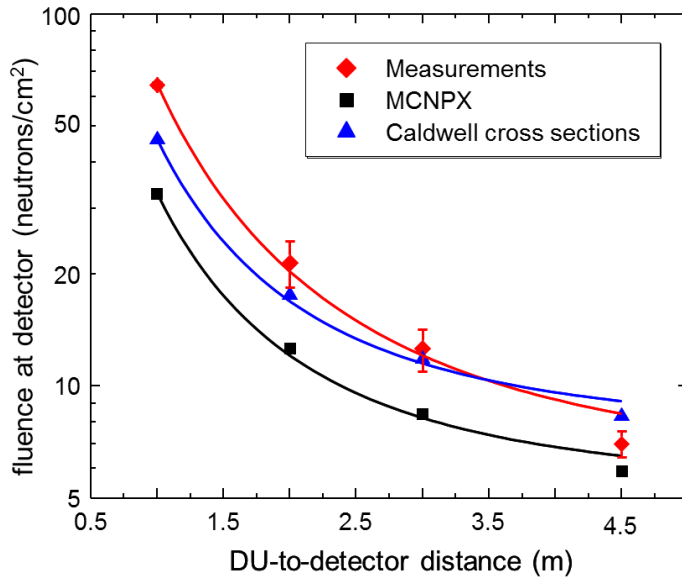


Figure 8. Comparison of the measured scaling of neutron intensity as a function of distance (red diamonds) with: calculations using MCNPX with its usual cross sections (black squares) and calculations using cross sections from Caldwell (blue triangles).

from Blohkin,⁴¹ calculated with a nuclear evaporation model. Calculations using measured cross sections from Caldwell,¹¹ shown as blue triangles in Fig. 8, are in closer agreement with the measurements. At photon energies below 9 MeV, the Caldwell cross sections are about two times larger than the Blohkin cross sections, but at higher energy these cross sections are similar. For the 8-MeV endpoint bremsstrahlung in these experiments, the measured cross sections of Caldwell give a better fit to the data. An inverse-square dependence supplemented by a constant term provides a reasonable fit to the results of measurements and MCNPX simulations (solid lines in Fig. 8). The inverse-square term represents direct neutron irradiation from the DU, whereas the constant term represents room-scattered neutrons. The parameters for these fits are listed in Table I. As shown in Table 1, the neutron fluence from MCNPX is about a factor of two smaller than the measurements, while calculations with the Caldwell cross sections are generally in better agreement with the measurements.

Table I. Fit parameters for scaling neutron fluence F with distance R (cm).

Data Source	Equation $F = A R^{-2} + B$	
	$A \text{ (cm}^2\text{)}$	$B \text{ (cm}^2\text{)}$
Measurements	59.3 ± 1.8	5.5 ± 0.9
MCNPX	27.8 ± 0.8	5.1 ± 0.4
Caldwell	38.9 ± 1.0	7.2 ± 0.5

include the quadratic combination of the statistical-counting uncertainty and the standard deviation of the average of three shots.

The scaling of these data is not inverse-square with distance. For example, the detector at 4.5 m measures more than twice the counts expected by inverse-square scaling from the detector at 1 m. Calculations of neutron scattering and absorption by the floor, walls, and ceiling using the MCNPX code provide an explanation for the measured scaling with distance.¹⁶

Results from calculations using two different photofission cross section sources also are shown in Fig. 8. MCNPX uses cross sections

It should be reiterated that these MCNPX computations used a forward-going bremsstrahlung spectrum corresponding to results from an LSP simulation with a constant 0.4% ion fraction for stimulated emission. Ion fraction values of 0.2-0.4% provide the best agreement with measurements of x-ray dose and fission-neutron yield when compared with predictions from ITS Cyltran computations of x-ray radiation transport to the DU plate and detectors.¹⁸ Other semi-analytic computations using the Caldwell cross sections and spectra for other ion fractions show that the neutron fluence versus distance is in good agreement with measurements for a slightly smaller ion fraction than 0.4%.¹⁸ This comparison is shown in Fig. 9 for four values of the ion fraction. The individual fluences for the three shots averaged in Fig. 8 are displayed in Fig. 9 with their values reduced by a constant 4.5 n/cm^2 to remove in an approximate way the room-scatter contribution.

Results show that a delayed neutron signature is detected that is consistent with simulations and analysis. The signal is significantly above induced background but the induced background must be invoked to explain the scaling of the neutron fluence with DU-to-detector distance. For the photon energies used here, the Caldwell photofission cross sections give better agreement with the data than the Blohkin cross sections used in MCNPX. A small ion current in the diode, associated with stimulated ion emission from the anode, is needed for the computed neutron fluences to agree with the measured neutron fluences. As will be seen in Sec 7, below, this small ion current is also needed to explain the angular distribution of the bremsstrahlung-producing electrons.

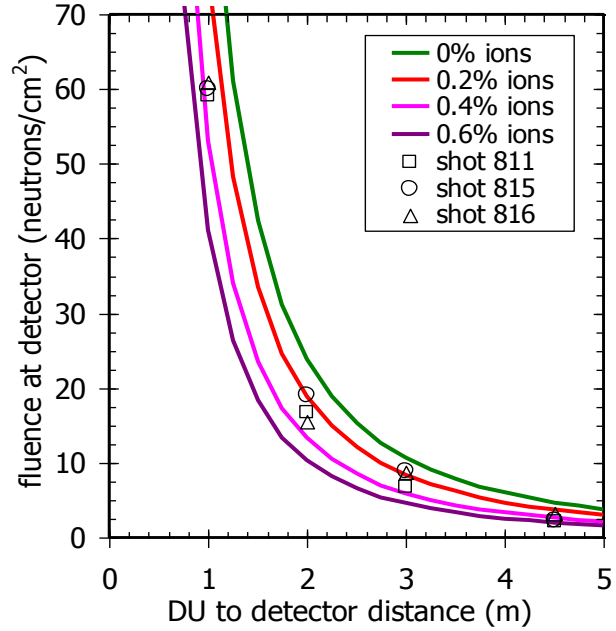


Figure 9. Room-subtracted fluence on the He-3 detectors vs distance from the DU plate compared with analysis using Caldwell cross-sections for 0% to 0.6% ion fractions. The fluences for the 3 displayed shots are averaged and plotted in the previous figure

5. PROMPT NEUTRON MEASUREMENTS

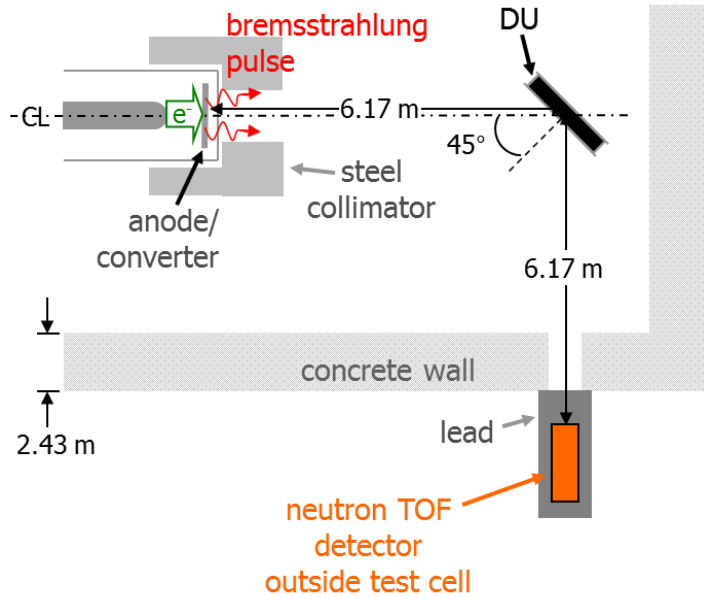


Figure 11. Top view of the bremsstrahlung diode, the DU object, and the neutron TOF detector for prompt neutron measurements.

the front face of the plate. The detector is located 6.17 m from the DU plate and is shielded with 14-cm (front) and 6-cm (sides) of lead to attenuate the intense bremsstrahlung scattered from the DU so that the photomultiplier tube can recover in time to respond to the energetic, prompt neutrons whose arrival to the scintillator are delayed by their TOF. The DU was replaced with a lead surrogate to compare the detector response to fission neutrons with the response to photonuclear neutrons from (γ, n) reactions in the lead surrogate.

Neutron TOF signals measured with the DU plate, the lead surrogate, and no object are compared in Fig. 11. With DU and lead, the initial pulses are of similar magnitude and recover to the baseline about 150 ns after the rise (the DU signal is obscured by the lead signal at this early time). With no object, this initial pulse is greatly reduced, consistent with this pulse being associated with

Prompt neutrons emitted from the DU plate were measured with a time-of-flight (TOF) detector mounted within a lead shield.⁴² The detector consisted of a 5.1-cm-diameter x 5.1-cm-thick plastic scintillator (BC408) optically coupled to a 5.1-cm diameter photomultiplier tube (XP2020). The arrangement is illustrated in Fig. 10. The detector is located outside the Mercury test cell and views the DU plate at 90° to the axis through a 15-cm-diameter hole in a 2.43-m thick ilmenite concrete wall. The DU is located on the generator axis 6.17 m from the tantalum converter and is rotated 45° to the incident bremsstrahlung direction so that the neutron detector views

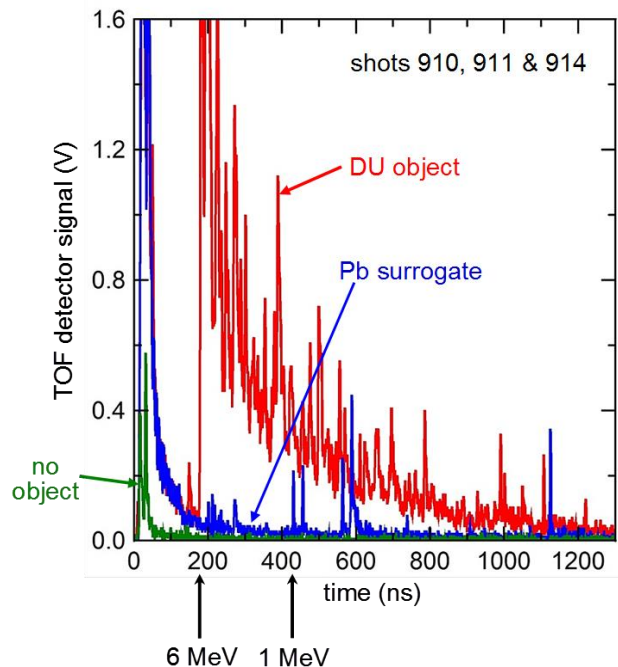


Figure 10. Measured neutron TOF detector signals for shot 910 with the DU object (red), for shot 911 with the lead surrogate (blue), and for shot 914 with no object (green).

scattered bremsstrahlung. Also, no neutron pulses are detected without an object. With the DU plate, a large signal from piled-up neutron pulses starts about 180 ns after the initial bremsstrahlung rise, corresponding to the maximum neutron energy from TOF of about 6 MeV. The initial piled-up neutron pulses are larger in amplitude than the later pulses, consistent with either higher energy neutrons, or more coincident neutrons reaching the detector early in time, or both. Fission-neutron energies may extend up to 10 MeV, while photonuclear neutrons from the $^{238}\text{U}(\gamma,n)^{237}\text{U}$ reaction with a 6.2-MeV threshold have energies less than 1.8 MeV for an 8-MeV endpoint bremsstrahlung spectrum. These measurements confirm that this TOF detector is measuring prompt fission neutrons from the DU. With the lead plate, many fewer pulses are recorded than with the DU plate. Most of these neutrons are consistent with less than 1.3-MeV photonuclear neutrons from the $^{207}\text{Pb}(\gamma,n)$ reaction, which has a 6.7-MeV threshold energy.

The few small pulses with lead between 200 and 300 ns correspond to higher TOF energies and cannot be so explained, though they are observed on all lead shots. One speculative explanation for these pulses in the 200-300 ns range is neutron TOF from high energy neutrons produced in the diode. From activation measurements on the Mercury center conductor, and rhodium activation foil measurements, we estimate that approximately 1 kA of ions are generated by the high-power e-beam striking the anode converter package. This is consistent with an ion fraction of about 0.5%, similar to those discussed in Secs. 4 and 7. These ions would predominantly originate from hydrocarbon contaminants on the anode surfaces. From isotopic ratios, approximately 100 mA of this ion current could be from deuterons, which would result in neutrons from the $^{27}\text{Al}(^2\text{H},n)^{28}\text{Si}$ reaction. This reaction has a positive Q-value (+9.36 MeV) and zero threshold, so it is possible for neutrons with 8 MeV (diode peak) + 9.37 MeV (Q-value) = 17.36 MeV to be produced. The lead surrogate would provide an excellent scattering location to direct some of these neutrons at the detector, and without the lead surrogate these neutrons would not be observed. The DU plate would also scatter these neutrons into the detector in a similar manner to the lead surrogate, but the detector response with DU is dominated by fission neutrons at this time, and the small diode neutron signal would not be distinguishable from the fission signature. The TOF for these neutrons would be ~220 ns. It must be stressed this explanation is a conjecture at this point and this mechanism must be studied in more detail to determine if the detector results are consistent with the predicted count rate vs time for this particular reaction, as well as for any other neutron-producing ion reactions that would also occur inside the diode.

The measured prompt neutron signal can be compared with the calculated neutron signal. As discussed previously in Sec. 4, the bremsstrahlung spectrum incident on the DU plate is calculated with LSP/ITS, and MCNPX is used to calculate the neutron incident on the scintillator. This MCNPX calculation is divided into two steps to reduce computation time. In the first step, irradiation of the DU by the computed bremsstrahlung spectrum is used to compute the output neutron spectrum from photofission and (γ,n) reactions. The second step determines the time-dependent neutron energy spectrum at the end of the hole in the 2.43-m thick concrete wall (shown in Fig. 10). A neutron spectral resolution of 100-keV is sufficient to resolve the 6.17-m TOF into 25-ns bins with a statistical precision better than 5%. The time profile of neutron emission at the DU is assumed to be a trapezoid with a base width of 40 ns: 12-ns rise, 13-ns flat top, and 15-ns fall. This trapezoid approximates the LSP/ITS bremsstrahlung intensity variation of photons above 5 MeV incident on the DU. Neutrons are tallied crossing the rear surface of the lead shield at the end of the 2.43-m long hole. No attempt is made to model the detector response in MCNPX. This calculation, in which a bremsstrahlung spectrum associated with 0% ions was used, indicates that 2.35×10^8 neutrons are emitted into the 2π steradians centered about the direction of the 15-cm diam hole in the wall leading to the TOF detector.

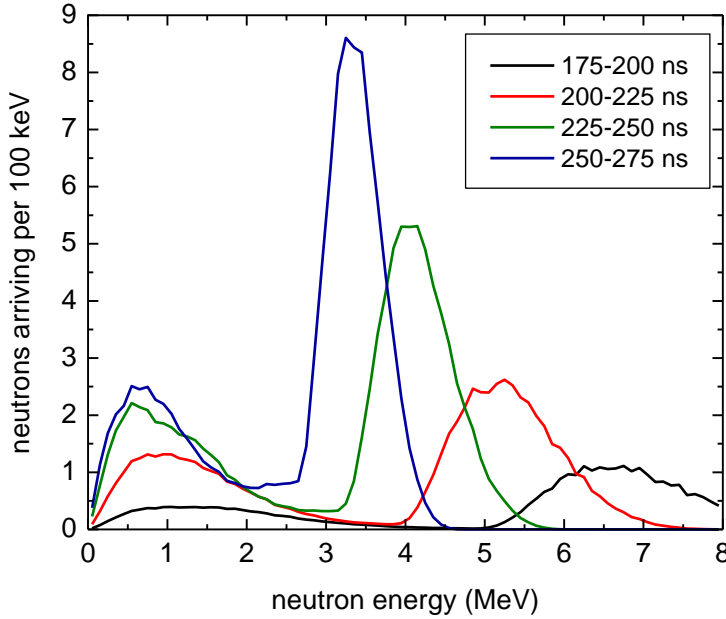


Figure 12. MCNPX-calculated neutron spectra for neutrons arriving at the TOF detector during the indicated time intervals. Time zero is at the beginning of prompt neutron emission from the DU.

Calculated average neutron spectra arriving at the TOF detector during four different 25-ns time bins are shown in Fig. 12. The most energetic neutrons arrive at the detector first, as expected. However, all of the spectra include a cluster of low-energy neutrons that result from scattering in lead and concrete during transport. Only about 2700 neutrons integrated over time and energy are transmitted through the lead into the vicinity of the neutron detector. About 300 neutrons are incident on the scintillator because the scintillator diameter is

only 5.1-cm compared with the 15-cm-diameter hole in the concrete wall. The number of neutrons detected is even smaller because of the efficiency of (n,p) scattering interactions in the scintillator. This small number of predicted neutrons is consistent with the TOF detector measurement.

The calculated neutron spectra averaged over 25-ns, $S_i(E_n)$, exemplified by the spectra in Fig. 12, are used to compute the shape of the TOF detector signal for comparison with a measurement. This comparison is quite challenging because of the complex nature of the measured TOF detector signal. The signal itself consists of piled-up pulses that cannot be deconvolved into countable pulses, and even for discrete pulses, the proton recoil mechanism and finite detector size severely limit the utility of using the deposited energy into the scintillator (pulse height) to infer the incident neutron energy for that event. However, for a detector operating strictly in the linear regime, for fast scintillation and light collection times compared to the signal timescale, and in the limit of many neutron detection events within the scintillator (such that an average energy deposition can be used to model each neutron detection event), we make the simplifying assumption that the detector signal can be interpreted as a current-mode measurement. Assuming that the detector response is proportional to the neutron energy, then $\int S_i(E_n) E_n dE_n$ is proportional to the number of neutrons detected in the i^{th} time interval. Under these assumptions, the current-mode measurement describes the neutron energy deposition as a function of time and is proportional to the computed energy deposition.

All of these weighted MCNPX spectrum integrals are combined to produce a computed approximate time history of the measured neutron TOF signal. The normalized, computed time history so obtained is compared with the measured TOF signal for shot 899 in Fig. 13. The experimental signal has been shifted by 20 ns relative to Fig. 11 to account for the x-ray flight time from the DU plate. The 5.08 cm dia. by 5.08 cm long scintillator satisfies the detector speed requirement. The detector linearity, which may ultimately be a reasonable approximation, is presently being investigated using neutron detection data taken from a Van de Graaff accelerator. The large event-number requirement within each time window is more difficult to assess. An

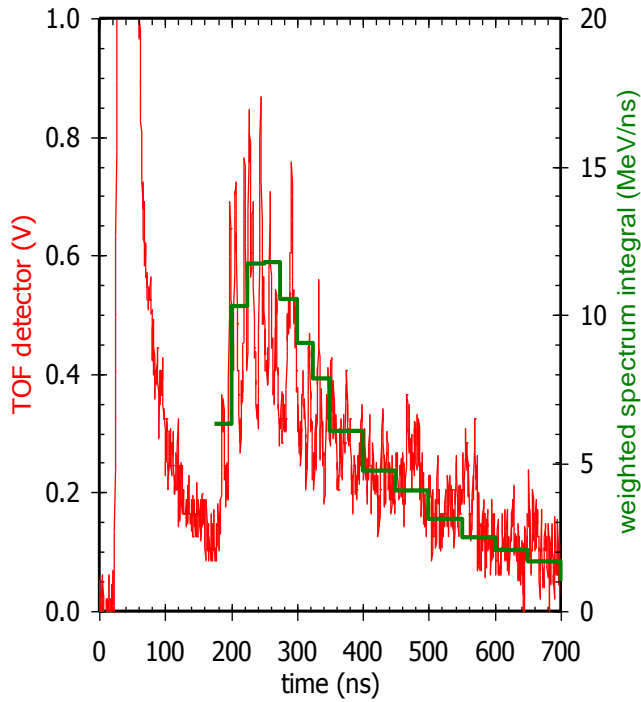


Figure 13. The calculated time history of the TOF response (green) from the weighted MCNPX-spectrum integrals is compared with the measured response (red) for the DU plate on shot 899, under several simplifying assumptions. The calculation is normalized to the measurement.

average detector signal over several shots could help satisfy this condition if more shots were available to analyze. The calculated neutron signature is consistent with the measured neutron detector response, and suggests that a current mode approximation is not out of the question for this diagnostic.

Results show that a prompt neutron signature with an appropriate TOF delay is measured when the bremsstrahlung source induces a fission response from the DU target. Under a set of simplifying assumptions, the computed time history is consistent with the measured TOF signal. When a lead surrogate replaces the DU target, the fission signature vanishes, as expected.

6. DETECTION STUDIES WITH MASS ATTENUATION

Experiments were carried out with various thicknesses and types of material interspersed between the DU plate and the Mercury bremsstrahlung source. The materials were lead, 2% borated polyethylene (BPE), and

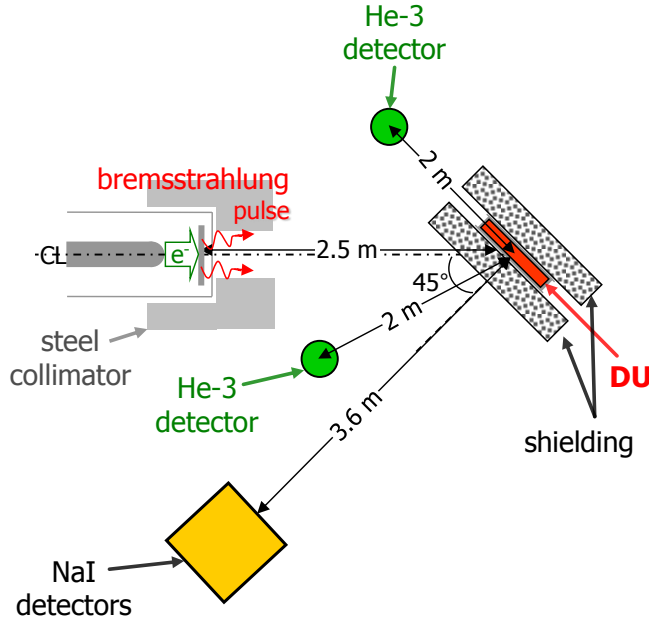


Figure 14. Top view of the bremsstrahlung diode, the NaI detectors and the He-3 detectors for measurements with attenuating material on the DU.

borated polyethylene (BPE), and a combination of both lead and BPE to determine the impact on the fission signature when the attenuation was a result of high-Z and low-Z materials. Both delayed γ -rays and delayed neutrons were measured as a function of the material thickness to account for the fact that lead attenuates γ -rays more efficiently than neutrons, while BPE attenuates neutrons more efficiently than γ -rays. As stated in Sec. 2, the AK gap for these measurements was 40 cm. The arrangement of the attenuation material, the DU plate, and the γ -ray and neutron detectors is presented in Fig. 14. The DU is located 2.5 m from the bremsstrahlung converter and is aligned at 45° so that the two radiation detectors view the

DU plate at near normal incidence. Delayed neutrons were measured using a single He-3 detector (described in Sec. 4) located 2.0 m from the DU. Delayed γ -rays were measured using the two large NaI:TI detectors (40.64-cm x 10.16-cm in area x 5.08-cm thick) placed 3.6 m from the DU and filtered in front with 0.63-cm thick lead and 5.08-cm thick BPE.

Measurements were made with three different types of attenuating-material configurations: lead only, BPE only, and both lead and BPE. Thicknesses were 1.27, 3.81, 6.35 and 10.16 cm for lead, and 5.24, 45.72, and 76.20 cm for BPE. For mixed lead and BPE, the thicknesses were 1.27-cm Pb + 15.24-cm BPE, 3.81-cm Pb + 45.72-cm BPE, and 6.35-cm Pb + 76.20-cm BPE with the lead always adjacent to the DU plate. These thicknesses are the actual thicknesses measured normal to the DU plate; they are not the thickness traversed by the interrogating bremsstrahlung (see Fig. 14). In all cases, the attenuating material was located on the front and back of the DU plate, as in a sandwich, and extended beyond the edge of the DU so that no bremsstrahlung is directly incident onto the DU. The counts recorded by each detector were summed over a time interval, and this sum is treated as a single measurement. For each configuration, two shots were taken and the results averaged.

Delayed γ -ray and delayed-neutron measurements are presented in Figs. 15 and 16, respectively, as a function of attenuation-material thickness in units of areal mass density, i.e., ρx in g/cm^2 , where ρ is the material density and x is the thickness traversed by the incident bremsstrahlung ($\sqrt{2}$ times larger than the thicknesses quoted above because of the 45° tilt of the DU plate relative to the machine axis). No attenuating material is used for the zero thickness data in Figs. 15 and 16. The uncertainty in each measurement is typically smaller than the size of the data point (a vertical solid line is used otherwise). For the delayed γ -ray measurements in Fig. 15,

only γ -rays recorded from 3 s to 5 s after the bremsstrahlung pulse and with energy between 3 and 7.5 MeV are included. This energy cutoff is chosen to avoid the ^{208}Tl γ -ray line at 2.614-MeV, as described in Sec. 3. The 3-s start-time for summing the counts is when the NaI detectors have fully recovered from the initial bremsstrahlung pulse. (Subsequent work has led to a much shorter recovery time.) For the neutron measurements in Fig. 16, pulses are summed from 1 ms to 1 s after the bremsstrahlung pulse. Again, the 1-ms start time is set by detector recovery from the bremsstrahlung pulse. Average active backgrounds, measured with no DU, are shown as dashed horizontal black lines in Figs. 15 and 16. These backgrounds include eight shots: two with only lead, two with only BPE, two with only a beryllium plate, and two with no object or

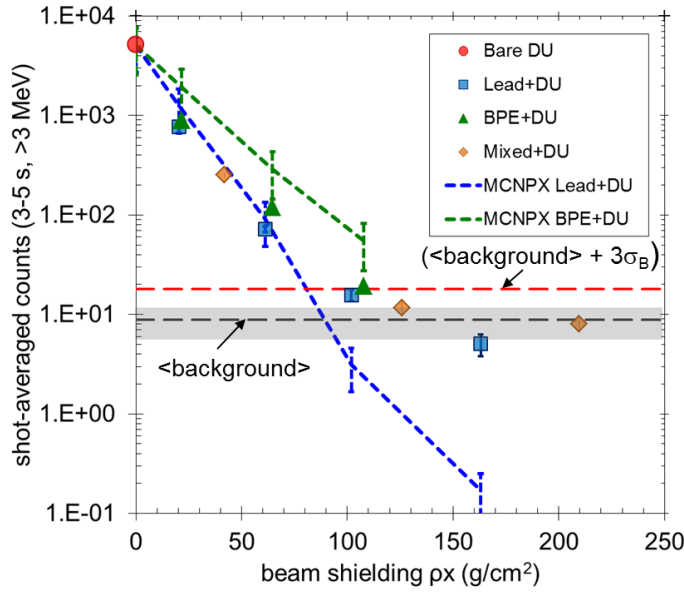


Figure 15. Delayed γ -ray measurements and results of MCNPX simulations for the different attenuating materials as a function of the material thickness expressed as areal mass density, ρx , where x is the distance traversed through the DU by the interrogating beam. The dashed lines are results from MCNPX simulations (normalized to zero ρx). The uncertainty in the data is within the size of the symbol except where a solid vertical line appears. The dashed vertical lines represent the $\pm 50\%$ confidence level for the simulations.

with neutron attenuation being dominated by the BPE.

The LSP/ITS and MCNPX codes were used in a manner similar to that described in Sec. 4 to calculate delayed γ -ray and delayed-neutron intensities with either lead or BPE sandwiching the DU plate. Results of these calculations are presented as dashed lines in Figs. 15 and 16 and can be compared with the measured counts. The estimated $\pm 50\%$ uncertainty in the MCNPX simulations is represented by vertical dashed lines at each ρx that was simulated. This uncertainty is primarily from uncertainties in the ^{238}U photofission cross section between 5 to 8 MeV (see Sec. 4). For the γ -ray results in Fig. 15, the calculated intensities are normalized to the measured counts with no attenuating material because the absolute response of the NaI detector has not been determined. It is interesting to note that the MCNPX simulations suggest a bigger difference in attenuation between high- and low-Z material than the measurements suggest. This discrepancy has not been resolved. For the neutron results in Fig. 16, the He-3-detector absolute response is known³⁹ and the MCNPX results are convolved with this response to obtain

attenuating material. The uncertainty in the backgrounds is the standard deviation, σ_B , for these eight shots and is indicated by the shaded regions in Figs. 15 and 16 (around the average background dashed line).

The γ -ray results in Fig. 15 for all three attenuation configurations follow a similar exponential decrease with increasing areal mass density. The measured decrease in γ -ray intensity with increasing areal mass density is only weakly dependent on the atomic number of the attenuating material. The neutron results in Fig. 16 demonstrate that the low-Z, BPE attenuates neutrons more efficiently than the high-Z lead for the same areal mass, as expected. The similarity of the results with BPE only and the mixed lead and BPE is consistent

the calculated data. The neutron counts determined in this way for both the lead and BPE attenuators are remarkably consistent with the measurements. The difference between the calculated and measured counts at zero thickness in Fig.

16 is still being investigated.

As the thickness of attenuating material is increased, the γ -ray and neutron fission signatures decrease so that detecting the presence of DU becomes more difficult. For the purposes of this work, three standard deviations above the active background ($3\sigma_B$), represented by the dashed red horizontal lines in Figs. 15 and 16, is used as a simplified measure of detection effectiveness for this idealized, laboratory setup. More sophisticated statistical treatments will be carried out in future work for more realistic active-detection scenarios. In Fig. 15, the delayed γ -ray count exceeds $3\sigma_B$ for ρx up to 100 g/cm² for all three types of attenuating-material configurations. In

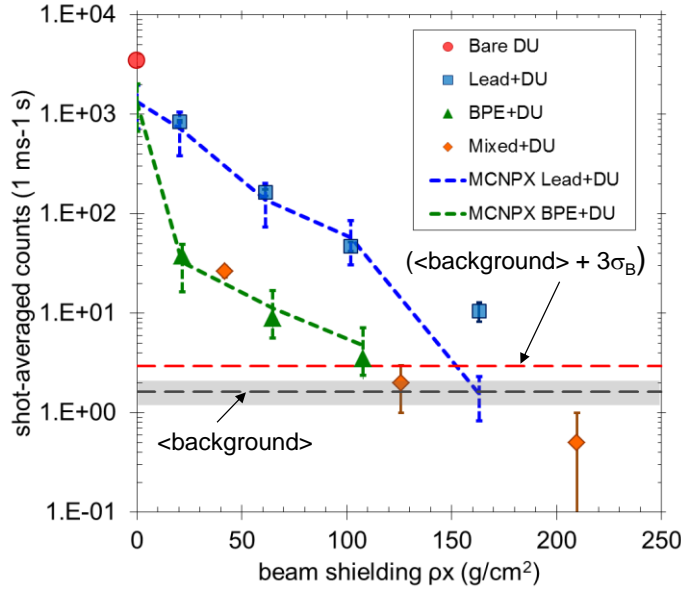


Figure 16. Delayed neutron measurements and results of MCNPX simulations for the different attenuating materials as a function of the material thickness expressed as areal mass density, ρx , where x is the distance traversed through the DU by the interrogating beam. The dashed lines are absolute results from MCNPX simulations. The uncertainty in the data is within the size of the symbol except when a solid vertical line appears. The dashed vertical lines represent the $\pm 50\%$ confidence level for the

Fig. 16, the delayed neutron count with lead exceeds $3\sigma_B$ for ρx up to 160 g/cm². Neutron measurements with BPE or mixed attenuating materials require a more detailed analysis because the sandwich nature of the attenuating material allows fission neutrons emitted through the uncovered edge of the DU plate to be room-scattered and reach the detector. In the future, ongoing analysis of this case will be augmented by experiments where attenuating material completely surrounds the DU plate.

Results show that attenuation with both high- and low-Z materials reduces the delayed γ -ray and delayed neutron signal produced from bremsstrahlung irradiation of a DU object. The attenuation of the measured delayed γ -ray signal is not very sensitive to the Z of the material and depends mostly on the areal mass density; whereas attenuation of the delayed neutron signal is considerably larger with low-Z material than with high-Z material. Simulations agree well with the measured neutron results. However simulations suggest the attenuation for delayed γ -rays is more sensitive to the Z of the attenuating material than indicated by the measurement, with the calculated attenuation by the low-Z material being somewhat less than the measurements suggest.

7. DIODE IMPROVEMENTS

To maximize the forward-going bremsstrahlung that induces fission in DU, electrons should impinge on the anode converter at as close to normal incidence as possible to take advantage of the preferentially forward directed bremsstrahlung (half angle $\sim 1/\gamma$, where γ is the relativistic factor for electrons). Also, their deposited charge at greater than about 6-MeV energy should be as large as possible. Both are of particular importance for long standoff applications, where the inverse-square-with-distance penalty can be very serious. In separate dedicated Mercury experiments, the fission yield from the DU plate was maximized by varying the diode AK gap between 23 and 43 cm and, for the larger gaps, by adding a 25-cm-long insert to reduce the inner diameter of the outer-conductor wall upstream of the converter.^{17, 43} As the AK gap increases the beam radius increases but the angle of incidence becomes closer to normal on the converter. The insert (not shown in Fig. 1, but illustrated in Fig. 17c) reduces the beam diameter at the converter while preserving near-normal incidence.^{17, 43} This insert was first described and used in Ref. 44 and was called an indented anode therein. An identical suite of diagnostics is fielded for each diode configuration. New current monitors on the anode at the downstream end of the insert (just before the anode end plate) determine the current actually reaching the bremsstrahlung converter. TLDs and an x-ray pinhole camera are used to measure the angular and radial x-ray dose distributions,^{43, 45} and He-3 detectors are used to measure fission yields induced in the DU plate

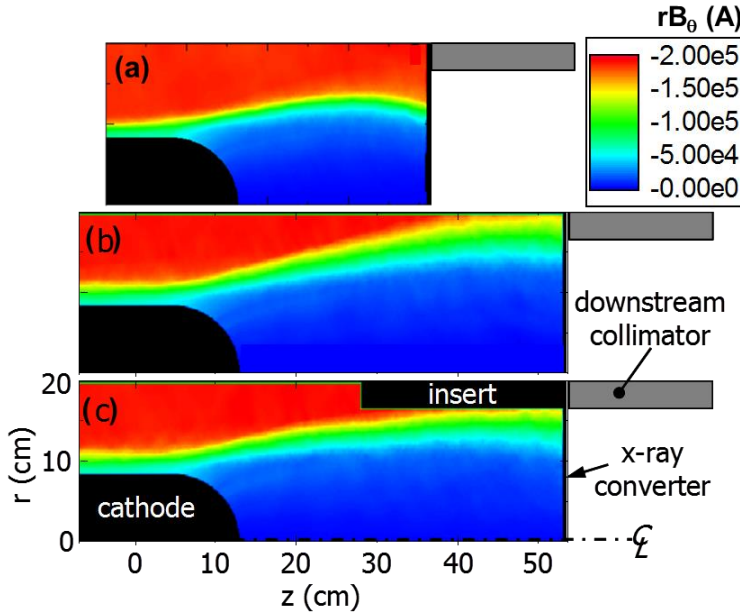


Figure 17. LSP rB_0 contours showing the enclosed current associated with electron flow in the Mercury diode for a) a 23-cm gap without an insert, b) a 40-cm gap without an insert, c) a 40-cm gap with an insert.

cm gap without the insert, and (c) a 40-cm gap with the insert. A stimulated ion emission fraction of 0.4% was used in all these simulations.

both on-axis and 15° off-axis.⁴³ All of these measurements are in broad agreement with LSP/ITS simulations of the electron dynamics and radiation transport for each diode configuration, which provides fundamental understanding of the processes contributing to fission-yield variations.⁴³

Simulations of the electron flow in the Mercury diode are illustrated in Fig. 17. There, LSP-computed rB_0 contours (i.e., current flow contours for azimuthally symmetric current flow) of the electron flow are shown for: (a) a 23-cm gap without the insert, (b) a 40-

In Fig. 18, the measured current entering the diode region (i.e., I_{load} of Fig. 2) is compared

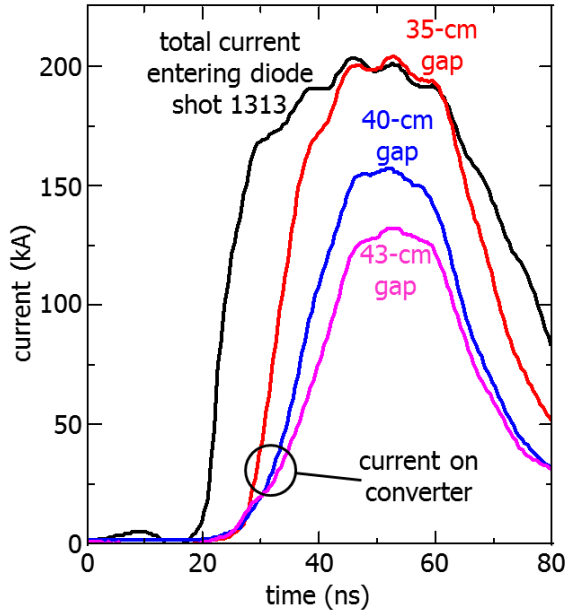


Figure 19. Electron current on the converter for 35-, 40-, and 43-cm AK gaps compared to the total current entering the diode region. For each gap, the current is a four-shot average and all shots have the indent installed. The total current is essentially the same for all gaps.

wall and insert persist for AK gaps larger than 35 cm, resulting in lower peak current on the converter for larger gaps.⁴³ This explanation is supported by x-ray pinhole images which show that the radial distribution of bremsstrahlung from the converter shifts to larger radius as the gap increases.⁴³

X-ray dose measurements also support this interpretation.^{43,45} Measurements of angular dose distributions at 1 m from the converter show a narrowing of angular spread with increasing AK gap, and a corresponding increase in on-axis dose as illustrated in Fig. 19. The insert is installed on all shots in Fig. 19 except the 23-cm-gap shots. For each gap, an average is taken over 4 or 5 sequential shots and displayed in the plot starting with shot 1295 for the 40-cm-gap case, shot 1301 for the 35-cm-gap case, shot 1323 for the 43-cm-gap case, and

with the measured current actually reaching the bremsstrahlung converter for 35-, 40-, and 43-cm AK gaps. The plotted converter currents are four-shot averages (typical variation is less than $\pm 10\%$) for each gap and all shots have the anode insert installed. The plotted total current, shown for a 35-cm gap (shot 1313), is nearly identical to the total currents for the other gaps. LSP simulations of the time-dependent electron flow in the diode for the different gaps are in agreement with the experimental results in Fig. 18. The delay in current rise at the converter compared to the total diode current is a result of early time electron losses to the outer conductor wall and to the insert as the e-beam transitions from an initially radial flow (to the outer wall) to an axial flow (to the bremsstrahlung converter and anode end plate). At peak current, however, the e-beam impinges on the anode at larger radius with increasing gap, so that some current loss to the outer

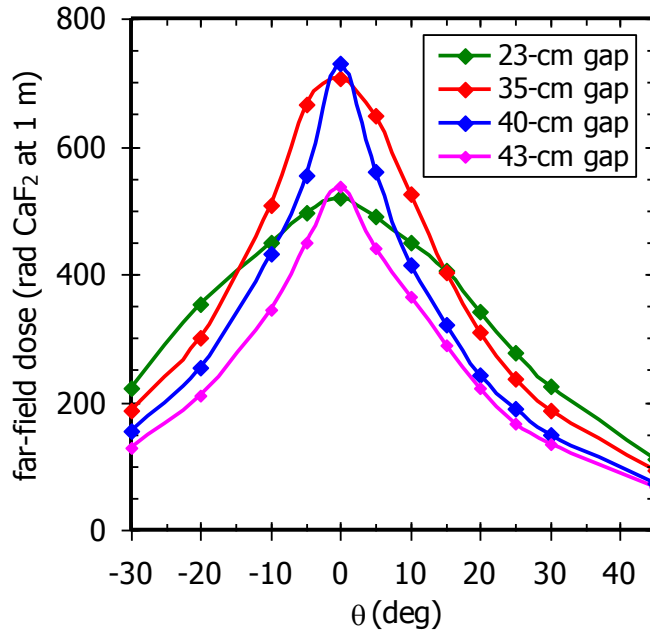


Figure 18. Shot-averaged angular dose distributions for various gaps. For each gap, the average is taken over 4 or 5 sequential shots. The 23-cm AK gap data was taken with no insert, while all other data were taken with an insert.

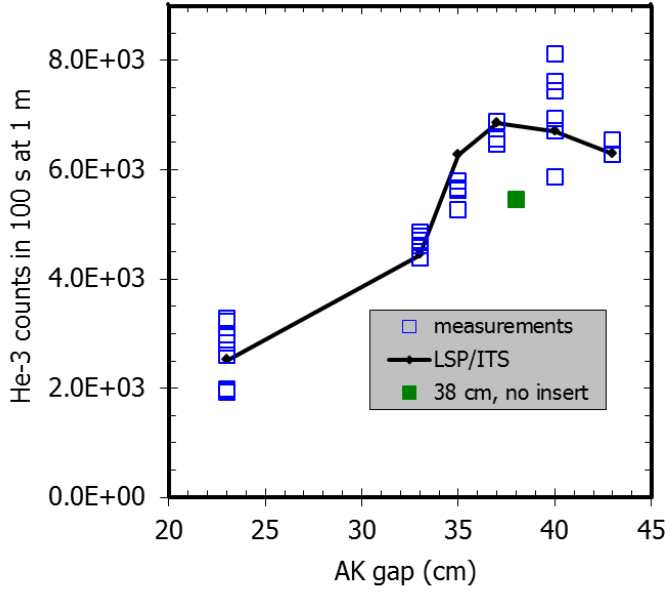


Figure 20. He-3 counts in 100 s for a detector 1 m from the DU plate. The black line is from LSP/ITS predictions. The 23- and 33-cm AK gap data and the one 38-cm-gap shot displayed as a solid green square were taken with no insert, while all other data were taken with an insert. The prediction assumes 8.9×10^4 fissions per He-3 count as determined from the computations described in the text.

configuration of Fig. 5 (i.e., to the left of the DU in the figure). The insert is not used on the shots with 23- and 33-cm AK gaps, but is used on the open-square data with gaps of 35 cm or larger. There is one 38-cm gap shot with no insert (solid-green square). The black line in Fig. 20 represents absolute-value predictions from LSP/ITS computations for the various diode configurations, assuming a 0.4% ion fraction, using the procedures outlined in the Sec. 4 to convert fissions in the DU to counts in the detector (i.e., each He-3 count corresponds to 8.9×10^4 fissions induced in the DU plate). The green-square datum at 38-cm AK gap (without an insert) indicates that for larger gaps where the neutron yield is larger, the yield is reduced without the insert. Increasing the AK gap from 23 cm to 40 cm and using the insert increases the neutron yield by a factor of three.

Predictions of electron angular distributions impacting the converter are shown in Fig. 21 for the LSP/ITS computations in Fig. 20.⁴³ These distributions produce x-ray angular divergences consistent with the dose measurements of Fig. 19 and, as shown in Ref. 43, neutron-yield measurements from an off-axis DU plate. Comparison of the dashed and solid 35-cm AK gap distributions indicates the improvement expected with the insert. With increasing AK gap, the computed electron angular distributions narrow and approach the converter at more normal incidence, and both the on-axis dose and the DU fission-neutron yield increase. For 40-cm gaps or larger, LSP electron-impact angles on the converter are within 5° of normal. For 8-MeV electrons, the x-ray divergence does not narrow significantly for smaller electron angles. Electron losses to the insert and wall continue to increase for larger gaps, however, explaining the reduced neutron yield at 43 cm in Fig. 20. If the current lost to the insert and walls could reach the converter, LSP/ITS predicts a fission yield 1.75-times larger than that achieved with a 40-cm gap. Though wall losses with a 23-cm gap are small, the predicted 20° electron impact angles produce only about 1/3 of the on-axis fissions of the 40-cm gap. Therefore, research has begun to

shot 1330 for the 23-cm-gap case. The behavior described above is attributed to electrons impacting the converter at angles closer to normal as the beam flows at larger radius.⁴³ This trend continues until the gap reaches 43 cm. At this value, electron losses to the outer wall and insert are large enough to reduce the on-axis dose. Shot-to-shot variations of the on-axis dose for the 23- through 40-cm-gap shots are about 5%, while that for the 43-cm gap is about 14%, demonstrating decreased reproducibility due to variable electron-beam losses to the insert and wall. The 23-cm-gap shots without the insert show the widest angular distribution.

Variation in delayed-neutron fission yield with increasing AK gap is shown in Fig. 20 for the He-3 detector located 1 m in front of the DU plate in the

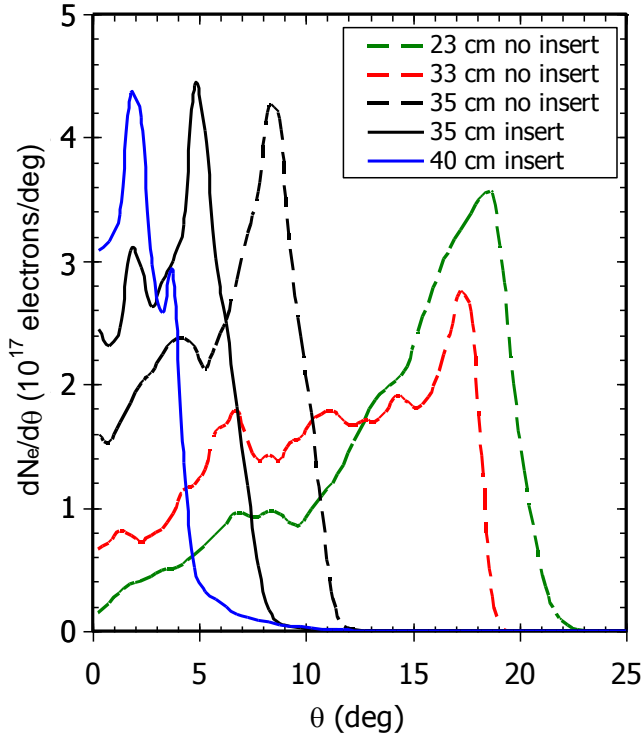


Figure 21. LSP predictions of electron angular distributions impacting the converter for various AK gaps and diode-load configurations.

modify smaller-gap diodes to magnetically steer electrons to converter impact angles closer to the normal.⁴⁶

Results show that the beam radius increases and the electron angular distribution becomes more normal to the converter as the AK gap increases. For a given AK gap, the insert also decreases the beam radius and narrows the angular distribution moving it closer to normal incidence. However, losses to the wall and insert eventual limit the benefit of these variations. By increasing the AK gap from the original 23 cm to 40 cm and installing the insert described above, an increase of a factor-of-three is achieved in the bremsstrahlung-induced fission yield from the DU plate.

8. SUMMARY AND CONCLUSIONS

The IPAD approach has several features that make it attractive for application to the active detection of fissile material. In the work reported here, we have demonstrated that a short, intense, bremsstrahlung pulse delivered to a DU plate at moderate endpoint energy can result in favorable conditions for measuring a variety of bremsstrahlung-induced fission signatures with acceptable active background and low-to-no passive background, even through a moderate-to-substantial amount of low-Z and high-Z attenuating material. We present early experimental results using the 8-MeV, 200 kA, 50-ns Mercury IVA at NRL, as well as results from analyses of these experiments and comparisons with simulations. The measurements and simulations are in general agreement, especially when more recent photo-fission cross sections are used. These measurements, simulations, and analyses demonstrate the principles of the IPAD approach. Demonstration of principles is not, however, demonstration of a capability. Real world conditions must be accounted for in any real application. In particular, the ~ 20 rad (CaF_2) dose could be considered prohibitively high for some applications. In that case, further work would be required to take full advantage of this IPAD approach that has the potential for the least amount of dose for given detection scenarios (be it for short-range or long-range applications) and given confidence levels.

Three different fission signatures from a 44-kg DU plate have been unambiguously measured: prompt neutrons using a fast TOF detector, delayed neutrons using appropriately filtered He-3 detectors, and delayed γ -rays using BGO and NaI detectors. Additionally, measurements of delayed neutrons and γ -rays have been carried out with three types of interspersed attenuating material: low-Z (BPE), high-Z (lead) and mixed-Z (BPE and lead). For our idealized, laboratory setup, the measured delayed- γ -ray counts equal or exceed 3 times the background standard deviation ($3\sigma_B$) for ρx up to 100 g/cm^2 for all three types of attenuating-material configurations. The delayed neutron counts with lead equal or exceed $3\sigma_B$ for ρx up to 160 g/cm^2 . Analyses and simulations of the measurements are in general agreement with these experimental results as well. Work is underway to improve on these results by decreasing the detector recovery time, thus being able to access any earlier and stronger fission signature that is not dominated by the induced background.

Finally, we have increased the fission yield by a factor of 3 with no change to the driving pulsed power by better control of the electron angles of incidence on the converter.

Future work will focus on varying the bremsstrahlung endpoint energy to explore the tradeoff between higher induced background and higher fission signal, carrying out experiments at large standoffs (10's of m),⁴⁷ reducing the recovery time of detectors to access more of the higher intensity portion of the fission signature, developing new methods for measuring prompt neutrons,⁴⁷ developing new approaches for manipulating the e-beam to maximize induced fissions without increasing the e-beam diameter,⁴⁶ investigating pulsed-power architectures that can reduce the size and weight of the pulsed-power driver,²⁰ and developing statistical approaches to quantify the probability of detection.

9. ACKNOWLEDGEMENTS

The authors wish to acknowledge the expert technical assistance of Mr. Aaron Miller, Mr. David Phipps, Mr. Eric Featherstone, and Mr. Anthony Culver. Without their considerable effort, this work would not have been possible. This work was funded by the Defense Threat Reduction Agency and the Office of Naval Research.

10. REFERENCES

1. T.B. Cochran and M.G. McKinzie, "Detecting nuclear smuggling," *Sci. Am.*, vol. 298, no. 4, pp. 98-104, April 2008.
2. See manuscripts in *Nucl. Instr. and Meth. in Phys. Res. B*, vol. 261, no. 1-2, pp. 268-378, August 2007.
3. T. Gozani, "Fission signatures for nuclear material detection," *IEEE Trans. on Nucl. Sci.*, vol. 56, no. 3, pp. 736-741, June 2009.
4. R.C. Runkle, D.L. Chichester, and S. J. Thompson, "Rattling nucleons: New developments in active interrogation of special nuclear material," *Nuc. Instrum. Meth. in Phys. Res. A*, vol. 663, no.1, pp. 75 - 95, January 2012.
5. M.T. Kinlaw and A.W. Hunt, "Time dependence of delayed neutron emission for fissionable isotope identification," *Appl. Phys. Lett.*, vol. 86, no. 25, pp. 254104-1-3, June 2005.
6. J.L. Jones, D.R. Norman, K.J. Haskell, J.W. Sterbentz, W.Y. Yoon, S.M. Watson, J.T. Johnson, J.M. Zabriskie, B.D. Bennett, R.W. Watson, C.E. Moss, and J.F. Harmon, "Detection of shielded nuclear material in a cargo container," *Nucl. Instrum. Meth. Phys. Res. A*, vol. 562, no.2, pp. 1085-1088, June 2006.
7. S.J. Thompson, M.T. Kinlaw, J.F. Harmon, D.P. Wells, E.B. Farfan, and A.W. Hunt, "Utilization of high-energy neutrons for the detection of fissionable materials," *Appl. Phys. Lett.*, vol. 90, no. 7, pp. 074106-3, February 2007.
8. J.L. Jones, D.R. Norman, K.J. Haskell, J.W. Sterbentz, W.Y. Yoon, L.G. Roybal, J.T. Johnson, S.M. Watson, M.T. Kinlaw, R.W. Watson, D.W. Gerts, N.O. Valles, M.C. Evans, M.P. Shannon, N.E. Hertel, K.L. Folkman, C.C. O'Neill, and A.W. Hunt, Idaho National Laboratory Report INL/EXT-09-15403, March 2009; and references therein.
9. John Stevenson, Tsahi Gozani, Mashal Elsalim, Cathie Condron, Craig Brown, "Linac based photofission inspection system employing novel detection concepts, *Nucl. Instrum. Meth. Phys. Res. A*, vol. 652, no. 1, pp. 124 – 128, October 2011.
10. M. Shannon, C. Vergien, P. Chapman, D. Wright, and J. Gronberg "ISIS Technology Development for Standoff Radiation Detection," *2012 HEART Conference* (Monterey, CA, March 2012).
11. J.T. Caldwell, E. J. Dowdy, B.L. Berman, R.A. Alvarez, and P. Meyer, "Giant resonance for the actinide nuclei: Photoneutron and photofission cross sections for ^{235}U , ^{236}U , ^{238}U , and ^{232}Th ," *Phys. Rev. C*, vol. 21, no. 4, pp. 1215 - 1231, April 1980.
12. S.B. Swanekamp, J.P. Apruzese, R.J. Commisso, S.L. Jackson, D. Mosher, J.W. Schumer, and James Jones, "A characterization of photon-induced activities generated by bremsstrahlung in the environment," *2011 IEEE Nuclear Science Symposium Conference Record (NSS/MIC)* (Valencia, Spain, October 2011).

-
13. S.B. Swanekamp, J.P. Apruzese, R.J. Commisso, S.L. Jackson, D. Mosher, J.W. Schumer, and James Jones, "A characterization of photon-induced activities generated by bremsstrahlung in the environment," *2012 HEART Conference* (Monterey, CA, March 2012).
 14. I.D. Smith, "The early history of western pulsed power," *IEEE Transactions on Plasma Science*, vol.34, no.5, pp.1585-1609, October 2006; and J.J. Ramirez, K.R. Prestwich, and I.D. Smith, "High-power, short-pulse generators based on induction voltage adders," *Proceedings of the IEEE*, vol. 80, no.6, pp. 946-957, June 1992.
 15. S.B. Swanekamp, J.P. Apruzese, R.J. Commisso, D. Mosher, and J.W. Schumer, "An analysis of intense pulsed active detection (IPAD) for the detection of special nuclear materials," *IEEE Trans. Nucl. Sci.*, vol. 58, no.4, pp. 2047 - 2054, August 2011.
 16. J.P. Apruzese, R.J. Commisso, J.W. Schumer, D. Mosher, S.B. Swanekamp, S.L. Jackson, D.D. Hinshelwood, F.C. Young, G. Cooperstein, and R.J. Allen, "Room scattering effects on the measured spatial distribution of delayed photofission neutrons from depleted uranium," *2011 IEEE International Conference on Plasma Science*, (Chicago, IL, June, 2011).
 17. D.D. Hinshelwood, R.J. Allen, J.P. Apruzese, R.J. Commisso, G. Cooperstein, S.L. Jackson, D. Mosher, D.P. Murphy, P.F. Ottinger, J.W. Schumer, S.B. Swanekamp, B.V. Weber, F.C. Young, A. Hunt, Z. Larsen, E. Cardenas, and A. Caruso, "High-power pulsed bremsstrahlung source for inducing photofission," *2011 IEEE International Pulsed Power Conference*, (Chicago, IL, June, 2011), pp 1428 - 1435.
 18. D. Mosher, J.W. Schumer, J.P. Apruzese, R.J. Commisso, D.D. Hinshelwood, S.L. Jackson, D.P. Murphy, and S.B. Swanekamp, "A computation-based analysis of photon-induced fission," *2011 IEEE International Pulsed Power Conference*, (Chicago, IL, June, 2011), pp. 1436-1441.
 19. I.D. Smith, P.A. Corcoran, R. Altes, D. Morton, R. Stevens, B. Whitney, R.J. Allen, R.J. Commisso, G. Cooperstein, and J.W. Schumer, "Evaluation of pulsed-power architectures for active detection," *2013 IEEE Pulsed Power & Plasma Science Conference*, (San Francisco, CA, 17 – 21 June 2013), pp. 1658-1663.
 20. P.A. Corcoran, I.D. Smith, R.G. Altes, R. A. Stevens, D.D. McGlathery, J.W. Pearce, R. J. Allen, R.J. Commisso, G. Cooperstein, F. Hegeler, J.W. Schumer, and J.D. Sethian, "A compact, transportable IVA concept for intense pulsed active detection," *2013 IEEE Pulsed Power & Plasma Science Conference* (San Francisco, CA, 2013).
 21. R.J. Commisso, J.W. Schumer, J.P. Apruzese, R.J. Allen, G. Cooperstein, D.D. Hinshelwood, S. L. Jackson, D. Mosher, D.P. Murphy, P.F. Ottinger, D.G. Phipps, S.B. Swanekamp, B.V. Weber, F.C. Young, A. Hunt, M.A. Gagliardi, and H.A. Seipel, "Development of an intense pulsed source of combined characteristic gamma rays and neutrons to induce fission," *2010 IEEE International Conference on Plasma Science*, (Norfolk, VA, June, 2010).
 22. S.L. Jackson, R.J. Allen, J.P. Apruzese, R.J. Commisso, D.D. Hinshelwood, D. Mosher, D.P. Murphy, P.F. Ottinger, J.W. Schumer, S.B. Swanekamp, F.C. Young, G. Cooperstein, A.W. Hunt, H.A. Seipel, and M.A. Gagliardi, "Detectors for intense, pulsed active detection," *2010 IEEE Nuclear Science Symposium Conference Record*, vol. N19-60, pp. 516-523, 2010; and in preparation for submission to *IEEE Trans. Nucl. Sci.*

-
- 23 B.J. Micklich, D.L. Smith, T.N. Massey, C.L. Fink, D. Ingram, "FIGARO: detecting nuclear materials using high-energy gamma-rays," *Nuclear Instruments and Methods in Physics Research A* vol. 505, no. 1-2 pp. 466–469, June 2003.
24. R.J. Allen, C.L. Berry, R.J. Comisso, G. Cooperstein, R.C. Fisher, D.D. Hinshelwood, T.A. Holt, A.T. Miller, D.P. Murphy, J.M. Neri, P.F. Ottinger, D.G. Phipps, J.W. Schumer, S.J. Stephanakis, S.B. Swanekamp, F.C. Young, D.L. Johnson, and I. Smith, "Initialization and operation of Mercury, a 6-MV MIVA (magnetically-insulated inductive voltage adder)," *2005 IEEE International Pulsed Power Conference*, (Monterey, CA, June 2005), p. 063501.
25. R.J. Allen, C.L. Berry, R.J. Comisso, E. Featherstone, R. Fisher, G. Cooperstein, D.D. Hinshelwood, S.L. Jackson, A.T. Miller, P.F. Ottinger, D.G. Phipps, and J.W. Schumer, "Conversion of Mercury (a 2-TW inductive voltage adder) to positive polarity," *2009 IEEE International Pulsed Power Conference*, (Washington, DC, June 2009), pp. 1171–1175.
26. D.D. Hinshelwood, P.F. Ottinger, J.W. Schumer, R.J. Allen, J.P. Apruzese, R.J. Comisso, G. Cooperstein, S.L. Jackson, D.P. Murphy, D. Phipps, S.B. Swanekamp, B.V. Weber, and F.C. Young, "Ion diode performance on a positive polarity inductive voltage adder with layered magnetically insulated transmission line flow," *Phys. Plasmas* vol. 18, no. 5, pp. 053106-1 – 053106-16, May 2011.
27. R.J. Allen, R.J. Comisso, G. Cooperstein, P.F. Ottinger, and J.W. Schumer, "Extension of the operating point of the Mercury IVA from 6 to 8 MV," *2011 IEEE International Pulsed Power Conference*, (Chicago, IL June 2011), pp. 1036 - 1041.
28. LSP is a software product of ATK Mission Research Corp., Albuquerque, NM 87110.
29. J.A. Halbleib, R.P. Kensek, G.D. Valdez, S.M. Seltzer, and M.J. Burger, "ITS: the integrated TIGER series of electron/photon transport codes - version 3.0," *IEEE Trans. on Nucl. Sci.*, vol. 41, no. 4, pp. 1025 - 1030, August 1992.
30. X-5 Monte Carlo Team, "MCNP – A general Monte Carlo N-particle transport code," Los Alamos National Laboratory Report, LA-UR-1987, 2005.
31. J.P. VanDevender, "Long Self-magnetically insulated power transport experiments," *J. Appl. Phys.*, vol. 50, no. 6, pp. 3928-3934, June 1979.
32. C.W. Mendel, "Planar one-dimensional magnetically insulated electron flow for arbitrary canonical-momentum distribution," *J. Appl. Phys.*, vol. 50, no. 6, pp. 3830-3837, June 1979.
33. C.W. Mendel, D.B. Seidel, and S.E. Rosenthal, "A simple theory of magnetic insulation from basic physical considerations," *Laser and Part. Beams*, vol. 1, no. 3, pp. 311-320, August 1983.
34. C.W. Mendel, and S.E. Rosenthal, "Dynamic modeling of magnetically insulated transmission line systems," *Phys. Plasmas*, vol. 3, no. 11, pp. 4207-4219, November 1996.

-
35. P.F. Ottinger and J.W. Schumer, "Rescaling of equilibrium magnetically insulated flow theory based on results from particle-in-cell simulations," *Phys. Plasmas*, vol. 13, no. 6, pp. 063109-1 – 063109-17, June 2006.
36. Aerodag is a registered trademark of Acheson Industries, Inc.
37. T.W.L. Sanford, J.A. Halbleib, J.W. Poukey, A.L. Pregonzer, R.C. Pate, C.E. Heath, R. Mock, G.A. Mastin, D.C. Ghiglia, T.J. Roemer, P.W. Spence, and G.A. Proulx, "Measurement of electron energy deposition necessary to form an anode plasma in Ta, Ti, and C for coaxial bremsstrahlung diodes," *J. Appl. Phys.* vol. 66, no. 1, pp. 10 - 22, July 1989.
38. M.T. Kinlaw, "Delayed neutron group parameters from photofission," Ph.D. dissertation, Dept. of Physics, Idaho State University, Pocatello, ID, December 2007, pp. 27-39.
39. S.B. Swanekamp, F.C. Young, S.L. Jackson, J.P. Apruzese, and R.J. Commisso, "Neutron detector designs for detecting fission neutrons in intense pulsed environments," *2011 IEEE Nuclear Science Symposium Conference Record (NSS/MIC)*, (Valencia, Spain, October 2011), pp. 363-369.
40. M.T. Kinlaw, "Delayed neutron group parameters from photofission," Ph.D. dissertation, Dept. of Physics, Idaho State University, Pocatello, ID, December 2007, pp. 18-26.
41. A.I. Blokhin, N.N. Buleeva, S.M. Nasyrova, O.A. Pakhomova, S.V. Zabroskaya, and A.M. Tsibulya, "Preparation and use of "BOFOD" evaluated photoneutron data library," IAEA International Nuclear Data Committee Report INDC(CCP)-381 (IAEA Nuclear Data Section, Wagramerstrasse 5, A-1400 Vienna, August 1994); originally published as A.I. Blokhin, A.N. Storozhenko, N.N. Buleeva, and M.V. Mikhailyukova, *Yadernye Konstanty*, vol. 3, pp. 3-54, 1992.
42. S.L. Jackson, R.J. Allen, J.P. Apruzese, R.J. Commisso, G. Cooperstein, D.D. Hinshelwood, D. Mosher, J.W. Schumer, S.B. Swanekamp, F.C. Young, J.C. Zier, A.W. Hunt, and E.S. Cardenas. "Detection of prompt neutrons from photofission induced by a single, intense bremsstrahlung pulse," *2011 Nuclear Science Symposium and Medical Imaging Conference*, (Valencia, Spain, Oct. 2011); and in preparation for submission to *IEEE Trans. Nucl. Sci.*
43. J.C. Zier, D. Mosher, R.J. Allen, R.J. Commisso, G. Cooperstein, D.D. Hinshelwood, S.L. Jackson, D.P. Murphy, P.F. Ottinger, A.S. Richardson, J.W. Schumer, S.B. Swanekamp, and B.V. Weber, "High-power, photofission-inducing bremsstrahlung source for intense pulsed active detection of fissile material," *Phys. Rev. ST Accel. Beams*. vol. 17, pp. 060401-1-060401-13, June 2014.
44. T.W.L. Sanford, J.A. Halbleib, J.W. Poukey, T.P. Wright, C.E. Heath, R. Mock, P.W. Spence, G. Proulx, V. Bailey, J. Fockler, and H. Kishi, "Improved bremsstrahlung radiation uniformity from an indented anode diode," *Appl. Phys. Lett.*, vol. 50, no. 13, pp. 809-811, March 1987.

-
45. D.P. Murphy, S.L. Jackson, J.C. Zier, D.D. Hinshelwood, R.J. Commisso, A.S. Richardson, J.W. Schumer, S.B. Swanekamp, D. Mosher, G. Cooperstein, and P.F. Ottinger, "X-Ray dose distribution measurements for electron-beam optimization on the Mercury inductive voltage adder," *2013 Pulsed Power Plasma Science Conference* (San Francisco, CA, June 2013).
46. S.B. Swanekamp, G. Cooperstein, D.D. Hinshelwood, D. Mosher, P.F. Ottinger, J.W. Schumer, B.V. Weber, and J.C. Zier, "Electron-Orbit Straightening Using a Post-Diode Magnetic-Field Structure for Large-Diameter Electron Beams," presented at *2013 IEEE Pulsed Power and Plasma Science Conference*. (San Francisco, CA, June 2013); and in preparation for publication.
47. B.V. Weber, R.J. Commisso, S.L. Jackson, D.P. Murphy, S.B. Swanekamp, and J.C. Zier, "Prompt Neutron Detection at Hermes-III," presented at *2013 IEEE Pulsed Power and Plasma Science Conference*. (San Francisco, CA, June 2013); and in preparation for publication.